Rigorous multi-slice wave optical simulation of X-ray propagation in inhomogeneous space.

Peter R. T. Munro[1,2]

[1]Department of Medical Physics and Biomedical Engineering, University College London, Gower Street, London WC1E 6BT, United Kingdom
[2]School of Electrical, Electronic & Computer Engineering, The University of Western Australia, Crawley, Western Australia 6009, Australia
[*]Corresponding author: p.munro@ucl.ac.uk

June 20, 2019

Abstract

The simulation of the propagation of divergent beams using Fourier-based angular spectrum techniques can pose challenges for ensuring correct sampling in the spatial and reciprocal domains. This challenge can be compounded by the presence of diffracting objects, as is often the case. Here, I give details of a method for robustly simulating the propagation of beams with divergent wavefronts in a coordinate system where the wavefronts become planar. I also show how diffracting objects can be simulated, whilst guaranteeing that correct sampling is maintained. These two advances allow for numerically efficient and accurate simulations of divergent beams propagating through diffracting structures using the multi-slice approximation. The sampling requirements and numerical implementation are discussed in detail and I have made the computer code freely available.

1 Introduction

The so-called multi-slice (MS) approximation has been widely used to perform wave optical simulations of beams propagating through diffracting structures too large for the projection approximation to be valid, see for example [1, 2, 3, 4, 5, 6], and is thus well established. The MS approximation instead divides the diffracting structure into a partition of slices to which the projection approximation may be applied individually. Algorithms employing the MS approximation generally use the theory of Fourier optics [7] to propagate beams across a slice between planes. Numerical implementations of such algorithms use the discrete Fourier transform (DFT) which make such algorithms computationally tractable. Careful attention must be paid to sampling in DFT based beam propagation techniques, which can become prohibitive when modelling divergent beams since correct sampling must be maintained in both the spatial and reciprocal spaces, throughout the entire simulated volume. This challenge can be exacerbated when modelling diffracting objects which may not be properly represented on a sampled grid. Despite the large number of published studies which employ the MS approximation, I am unaware of any which have analysed, or proposed a solution to, the challenge posed by sampling divergent beams in a MS simulation containing diffracting objects. A method of transforming a divergent beam geometry into a plane wave geometry for single slice simulation has been demonstrated [8, 9, 6]. In this paper I provide a full description of how to integrate this transformation into a MS simulation in order to calculate how a coherent divergent beam propagates through a diffracting sample extended in the axial direction. Furthermore, I provide a thorough analysis of the sampling requirements of this new approach and show how it can be implemented in such a way that guarantees that correct sampling is maintained throughout the simulation.

I begin this paper with an overview of preliminary theory required to develop the simulation technique, including angular spectrum approaches to propagating beams within a system described by the paraxial wave equation. The sampling requirements of this technique, in both the spatial and reciprocal spaces, are reviewed before describing how diffracting objects are treated. I then introduce the divergent-wave to plane-wave transformation which allows for significant relaxation of the sampling requirements. It is then shown how this transformation can be applied in the MS approximation and provide details of its numerical implementation and sampling requirements. I conclude the paper with a series of examples which provide verification of the new simulation method and illustrate its usefulness.

1.1 Preliminary theory

I consider a system as depicted in Fig. 1 where a monochromatic point source is located at the origin of the global coordinate system. Extended sources which are spatially incoherent can be represented by collections of point sources and polychromatic sources may be modelled by incoherently superimposing simulations performed at wavelengths throughout the source spectrum. Although beyond the scope of this paper, sources with more general states of coherence may be

modelled by performing one simulation for each mode of the source's coherent mode decomposition. I assume that free space exists for $0 \leq z \leq \Delta z_{so}$, where I use the subscript so to denote source to object distance. I also assume that some degree of refractive index inhomogeneity exists in the region $z \geq \Delta z_{so}$ and that our ultimate goal is to calculate the field in the plane $z = \Delta z_{so} + \Delta z_{od}$, where Δz_{od} is the object to detector distance. I thus refer to the space defined by $\Delta z_{so} \leq z \leq \Delta z_{so} + \Delta z_{od}$ as the computational region. I describe fields propagating in this system according to the form $u(x, y, z) \exp(\mathrm{i}kz - \mathrm{i}\omega t)$, where k is the wavenumber , ω is the angular frequency of the radiation emitted by the source and it is assumed that $u(x, y, z)$ varies only weakly with z. If $u(x, y, z) \exp(\mathrm{i}kz - \mathrm{i}\omega t)$ is substituted into the time-harmonic scalar wave equation, it is not difficult to show that the paraxial wave equation is obtained as:

$$\frac{\partial^2 u}{\partial x^2} + \frac{\partial^2 u}{\partial y^2} + 2\mathrm{i}k\frac{\partial u}{\partial z} = 0. \tag{1}$$

The angular spectrum, $U(a, b, z)$, associated with a wavefield, $u(x, y, z)$, can be used to propagate such a field over some axial distance in a homogeneous space. It has been shown that $u(x, y, z)$ and $U(a, b, z)$ are related according to [7]:

$$U(a, b, z) = \iint_{-\infty}^{\infty} u(x, y, z) \exp(-\mathrm{i}2\pi(x(a/\lambda) + y(b/\lambda)))\mathrm{d}x\mathrm{d}y \tag{2}$$

$$u(x, y, z) = \iint_{-\infty}^{\infty} U(a, b, z) \exp(\mathrm{i}2\pi(x(a/\lambda) + y(b/\lambda))) \cdot \mathrm{d}\left(\frac{a}{\lambda}\right)\mathrm{d}\left(\frac{b}{\lambda}\right). \tag{3}$$

It is then relatively straight forward to show that a component of an angular spectrum may be propagated a distance Δz in homogeneous space according to [7]: $U(a, b, z + \Delta z) = P(a, b, \Delta z)U(a, b, z)$, where

$$P(a, b, \Delta z) = \exp(-\mathrm{i}k(a^2 + b^2)\Delta z/2) \tag{4}$$

is the well known free space propagation operator.

The spherical wave emitted by the point source has complex amplitude in the free space region of $\exp(\mathrm{i}kr)/r$, where $r = \sqrt{x^2 + y^2 + z^2}$. If I make the Fresnel approximation to this field and drop the $\exp(\mathrm{i}kz)$ dependence, I obtain the expression:

$$u_{inc}(x, y, z) = \exp\left(\mathrm{i}k(x^2 + y^2)/(2z)\right)/z, \tag{5}$$

which satisfies the paraxial wave equation, Eq. (1).

Our objective in this paper is to employ discrete Fourier transform (DFT) techniques to determine the complex amplitude which emerges from the plane $z = \Delta z_{so} + \Delta z_{od}$ when refractive index inhomogeneities may exist in the region $z \geq \Delta z_{so}$. The principal limitation when using DFT based techniques is that the field must at all times be sampled in a manner which satisfies the Nyquist criterion. When considering spherical waves, impractically dense sampling requirements may result . Since the main aim of this paper is to avoid such dense sampling, I first show how these dense sampling requirements arise from Eq. (5). In particular, if one writes u_{inc} as:

$$u_{inc}(x, y, z) = \exp(\mathrm{i}\phi(x, y, z))/z, \tag{6}$$

the local spatial frequencies may be defined as [7]:

$$f_{inc,x} = \frac{1}{2\pi}\frac{\partial}{\partial x}\phi(x, y, z) = \frac{x}{\lambda z} \tag{7}$$

$$f_{inc,y} = \frac{1}{2\pi}\frac{\partial}{\partial y}\phi(x, y, z) = \frac{y}{\lambda z}. \tag{8}$$

However, A further constraint on sampling arises after calculating the angular spectrum of u_{inc} using Eq. (2) which gives:

$$U_{inc}(a, b, z) \quad = \quad \mathrm{i}\lambda \exp(-i(a^2 + b^2)kz/2), \tag{9}$$

which must also be sampled according to the Nyquist criterion. By following the same procedure as was used to derive Eqs. (7) and (8), I can obtain the following expressions for the local frequency content of the angular spectrum:

$$f_{inc,a} = \frac{az}{\lambda} \tag{10}$$

$$f_{inc,b} = \frac{bz}{\lambda}. \tag{11}$$

In any DFT based field propagation technique, discrete spatial coordinates and propagation vectors must be defined. I denote these by $(\tilde{x}, \tilde{y})$ and $(\tilde{a}, \tilde{b})$, respectively. Furthermore, for simplicity, in the remainder of this manuscript I will assume that $\tilde{x} = \tilde{y}$ and $\tilde{a} = \tilde{b}$. Then, if I have N (assumed even without loss of generality) sample points for each such quantity, these discrete coordinates may be defined as:

$$\tilde{x} = \tilde{y} = \{(j - N/2)\Delta x | 0 \leq j < N\} \tag{12}$$

$$\tilde{a} = \tilde{b} = \{\lambda(j - N/2)/(N\Delta x) | 0 \leq j < N\}. \tag{13}$$

For this analysis only I shall neglect the additional complication arising from the implicit periodicity in N underlying the DFT. This discretisation must satisfy the Nyquist criterion in both the spatial and reciprocal spaces. In particular, $\Delta x = \Delta y$ and $\Delta a = \Delta b$ must satisfy:

$$\Delta x \leq \frac{1}{2\max\left(|f_{inc,x}|\right)} \tag{14}$$

$$\Delta a \leq \frac{1}{2\max\left(|f_{inc,a}|\right)}, \tag{15}$$

where $\max(f)$ is taken to mean the maximum value of f. Equations (12) and (13) reveal that $\max(x) = \Delta x N/2 = X$ and $\max(a) = \lambda/(2\Delta x) = A$ which allows, with the aid of Eqs. (7) and (10), us to write:

$$\max\left(|f_{inc,x}|\right) = \frac{\Delta x N}{2\lambda \Delta z_{so}} \tag{16}$$

$$\max\left(|f_{inc,a}|\right) = \frac{\Delta z_{so} + \Delta z_{od}}{2\Delta x}. \tag{17}$$

In order to proceed it is assumed that N is fixed and that Δx may be varied to achieve correct sampling. Then, by substituting Eqs. (16) and (17) into Eqs. (14) and (15), respectively,

and using the relationship $\Delta a = \lambda/(N\Delta x)$, the following inequalities are obtained, which must be satisfied if the Nyquist criterion is to be satisfied in both the spatial and reciprocal spaces:

$$\Delta x \leq \sqrt{\frac{\lambda \Delta z_{so}}{N}} \tag{18}$$

$$\Delta x \geq \sqrt{\frac{\lambda(\Delta z_{so} + \Delta z_{od})}{N}}, \tag{19}$$

which are unable to be satisfied simultaneously. Equation (18) states that since N is fixed, the transverse width of the simulation must not exceed a particular value if the field incident upon the computational volume is to be sampled correctly in the spatial domain. Equation (19), however, states that in order to correctly sample the angular spectrum in the reciprocal space for fixed N, at some plane beyond the computational volume entrance plane, the transverse width of the simulation must exceed a particular value. The problem arises because these two constraints cannot be satisfied simultaneously.

The final aspect of preliminary theory deals with inhomogeneous refractive index distributions, which I treat using the so-called projection approximation [10, 6]. I explain this with the aid of Fig. 1 which contains a position dependent refractive index distribution, within the region $z_i \leq z \leq z_{i+1}$, described by:

$$n(x, y, z) = 1 - \delta(x, y, z) + \mathrm{i}\beta(x, y, z). \tag{20}$$

Under the projection approximation it is assumed that if the field exiting the region $z_i \leq z \leq z_{i+1}$, in the absence of a refractive inhomogeneity, is given by $u(x, y, z_{i+1})$, the perturbed field is given as $u(x, y, z_{i+1}) \exp(\mathrm{i}\phi(x, y))$, where

$$\phi(x, y) = k \int_{z_i}^{z_{i+1}} (-\delta(x, y, z) + \mathrm{i}\beta(x, y, z))\mathrm{d}z, \tag{21}$$

and k is the free space wavenumber. In obtaining this result it is assumed that, outside of the support of the refractive index inhomogeneity, $\delta(x, y, z) = 0$ and $\beta(x, y, z) = 0$. Typical implementations of the MS method work by partitioning the volume containing a diffracting structure into slices, as depicted in Fig. 2, such that the $(i + 1)$th slice is defined by $z_i \leq z \leq z_{i+1}$. The field exiting the plane $z = z_{i+1}$ is first calculated assuming the slice $z_i \leq z \leq z_{i+1}$ is composed of free space. This is performed by calculating the angular spectrum of the field $u(x, y, z_i)$ according to Eq. (2), propagating the angular spectrum to the end of the slice using the free space propagation operator (Eq. (4)), before evaluating the field at $z = z_{i+1}$, $u(x, y, z_{i+1})$, using Eq. (3). Refractive index inhomogeneity in the slice is then accounted for by multiplying $u(x, y, z_{i+1})$ by $\exp(\mathrm{i}\phi(x, y))$ where $\phi(x, y)$ is evaluated according to Eq. (21). This procedure is then repeated until the field at $z = \Delta z_{so} + \Delta z_{od}$ is obtained.

1.2 Divergent beam to plane wave transformation

The sampling requirements expressed in Eqs. (18) and (19) for modelling divergent spherical waves cannot be achieved simultaneously. However, they can be circumvented by applying a coordinate system transformation which transforms the divergent spherical wave into a plane wave [8, 9, 6]. Although this subject is treated in detail by Paganin [6], I follow here the notation introduced by Sziklas and Siegman [8, 9]. I introduce this transformation by considering the problem depicted in Fig. 1 whereby the complex amplitude incident upon the plane $z = z_i$ is known, which I denote by $u(x, y, z_i^-)$. Consider for now that the space $z_i \leq z \leq z_{i+1}$ is composed only of homogeneous space, i.e., there is no refractive index inhomogeneity present within the slice. I note that two coordinate systems are depicted in this diagram: the global coordinate system (x, y, z) and a coordinate system (x_i', y_i', z_i'), valid only for $z_i \leq z \leq z_{i+1}$. In order to evaluate $u(x, y, z_{i+1}^-)$, I first perform a transformation into a primed coordinate system defined by [8, 9]:

$$u(x, y, z_i) = \exp\left(\mathrm{i}k(x^2 + y^2)/(2z_i)\right) v(x_i', y_i', z_i')/z_i \tag{22}$$

$$x_i'(x, z) = \frac{x}{M_i} \tag{23}$$

$$y_i'(x, z) = \frac{y}{M_i} \tag{24}$$

$$z_i'(z) = \frac{z - z_i}{M_i}, \tag{25}$$

where $M_i(z) = z/z_i$. It is clear from Eqs. (22)-(25) that at $z = z_i$ I have $x_i'(x, z_i) = x$, $y_i'(y, z_i) = y$ and $z_i'(z_i) = 0$, thus the transverse coordinates are identical. Furthermore, it is straightforward to show that $v(x_i', y_i', z_i')$ satisfies the paraxial wave equation (Eq. (1)) in the primed coordinate system. This means that techniques, such as angular spectrum propagation, developed for calculating the propagation of fields which satisfy the paraxial wave equation can be applied to $v(x_i', y_i', z_i')$ instead of $u(x, y, z)$. This overcomes the sampling problem expressed by Eqs. (18) and (19) since a divergent spherical wave in the global coordinate system becomes a plane wave in the primed coordinate system.

Having obtained $v(x_i', y_i', z_i'(z_i) = 0)$ from Eq. (22) it remains to calculate $v(x_i', y_i', z_i'(z_{i+1}))$ using angular spectrum propagation. I begin by calculating the angular spectrum of $v(x_i', y_i', 0)$ using Eq. (2) thus giving $V(a_i, b_i, 0)$, which can be propagated a distance $z_i'(z_{i+1})$ according to Eq. (4) as:

$$V(a_i, b_i, z_i'(z_{i+1})) = P(a_i, b_i, z_i'(z_{i+1}))V(a_i, b_i, 0) \tag{26}$$

where, from Eq. (25), $z_i'(z_{i+1}) = (z_{i+1} - z_i)/M_i(z_{i+1})$ and $M_i(z_{i+1}) = z_{i+1}/z_i$. The complex amplitude in the primed coordinate system can thus be obtained by applying Eq. (3) to $V(a_i, b_i, z_i'(z_{i+1}))$ thus giving $v(x_i'(x, z_{i+1}), y_i'(y, z_{i+1}), z_i'(z_{i+1}))$. The complex amplitude in the global coordinate system is found by inverting the coordinate system transformation expressed in Eqs. (22)-(25) which

will result in:

$$u(x,y,z_{i+1}) = \exp\left(\mathrm{i}k(x^2+y^2)/(2z_{i+1})\right)\frac{v(x_i',y_i',z_i'(z_{i+1}))}{z_{i+1}} \tag{27}$$

$$x = (z_{i+1}/z_i)x_i'(x,z_{i+1}) = M_i(z_{i+1})x_i'(x,z_{i+1}) \tag{28}$$

$$y = (z_{i+1}/z_i)y_i'(y,z_{i+1}) = M_i(z_{i+1})y_i'(x,z_{i+1}) \tag{29}$$

$$z = z_{i+1}, \tag{30}$$

which illustrates how returning from the primed (i.e. local) coordinate system to the global coordinate system entails a magnification of the transverse coordinates. Having obtained $u(x,y,z_{i+1})$, the procedure outlined above may be repeated to propagate the complex amplitude from the plane $z = z_{i+1}$ to the plane $z = z_{i+2}$ and so on.

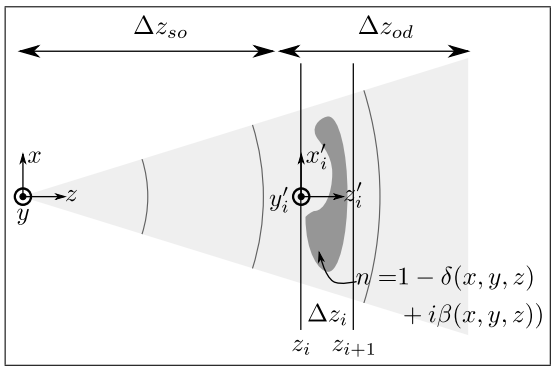

Figure 1: Schematic diagram of the system studied in this manuscript. A point source is located at the origin of the Cartesian coordinate system. Refractive index inhomogeneities may exist for $z > \Delta z_{so}$, one example of which is illustrated in a layer bounded by the planes $z = z_i$ and $z = z_{i+1} = z_i + \Delta z_i$.

1.3 Simulation of an inhomogeneous refractive index distribution

I use the projection approximation discussed in Sec. 1.1 to model refractive index inhomogeneities present within the slice $z_i \leq z \leq z_{i+1}$. The projection approximation can be applied in either the global or primed coordinate systems due to the linearity of Eq. (22). I opt to apply the projection approximation directly in the primed coordinate system, i.e., I apply it directly to $v(x_i',y_i',z_i'(z_{i+1}))$, where I have dropped the dependence of x_i' and y_i' on (x,z) and (y,z), respectively, for brevity. It is important to note, however, that I must transform the argument of the projection function (Eq. (21)) from the global to the primed coordinate system. In particular, the projection approximation must be applied as $v(x_i',y_i',z_i'(z_{i+1}))\exp(\mathrm{i}\phi(M_ix_i',M_iy_i'))$ when operating in the primed coordinate system. Whilst this is evident from the transformation expressed in Eqs. (22)-(25), this may be understood intuitively by noting that the lateral cross-section of an object must effectively be de-magnified in the primed coordinate system to compensate for the lack of divergence in the incident wavefront. However, despite this de-magnification, its optical thickness must remain the same in both coordinate systems.

1.4 Mitigating aliasing due to use of discrete Fourier transforms

Even after applying the divergent to plane wave transformation, aliasing, due to the use of discrete Fourier transforms, may still result due to the presence of diffracting refractive index inhomogeneities. In particular, the projection function $\exp(\mathrm{i}\phi(x,y))$ will not, in general be band limited. Thus, if a complex amplitude in the absence of a diffracting object, $v(x',y',z')$, is band limited, the complex amplitude after the application of the projection approximation $v(x',y',z')\exp(\mathrm{i}\phi(M_ix_i',M_iy_i'))$ will not be, in general. I suggest an approach to overcoming this problem by calculating a band limited projection function. This approach is only possible for diffracting objects for which the Fourier transform of its projection function can be calculated either analytically or numerically to high precision. Suppose I define a projection function $t(x,y) = \exp(\mathrm{i}\phi(x,y))$, I define the band limited version of $t(x,y)$ as:

$$t_{\mathrm{BL}}(\tilde{x},\tilde{y}) = \hat{\mathcal{F}}^{-1}\{W(\tilde{f}_x,\tilde{f}_y)T(\tilde{f}_x,\tilde{f}_y)\}, \tag{31}$$

where t_{BL} is the band limited version of t, W is a windowing function, $T(f_x,f_y) = \mathcal{F}\{t(x,y)\}$, $\hat{\mathcal{F}}$ is the discrete Fourier transform operator and $\mathcal{F}$ is the continuous Fourier transform operator. I note here that is convenient to introduce the spatial frequency parameters $(f_x,f_y) = (a/\lambda, b/\lambda)$. Variables under the tilde sign are assumed to be discretised. A variety of windowing functions could be used, however, in this work a Tukey window was employed.

It is worth noting that for many applications this step may be omitted without significantly perturbing the calculation of the transmitted complex amplitude, as many other implementations of the multi-slice method do. This approach is presented here as a means of eliminating aliasing for applications where this is important.

2 Calculation of field propagating through an arbitrary number of slices

Consider the geometry depicted in Fig. 2 where the space $z_0 \leq z \leq z_{N_s}$ is divided into N_s slices. Propagation from the plane $z = z_0$ to the plane $z = z_{N_s}$ can be achieved by performing N_s individual propagation calculations between the planes indicated in Fig. 2. When using the divergent beam to plane wave transformation, it is important to note that a different transformation is required for each slice. The details of these transformations are indicated in Fig. 2. I denote the primed coordinate system in a particular slice by the subscript associated with the plane closest to the source. For example, the primed coordinate system corresponding to the region $z_i \leq z \leq z_{i+1}$ is denoted (x_i',y_i',z_i'). Propagation through the first slice (i.e., the slice defined by $z_0 \leq z \leq$

z_1) is achieved by evaluating $v(x_0', y_0', 0)$ according to Eqs. (22)-(25), giving the field in the primed coordinate system at $z = z_0$. Under this transformation the primed and global coordinate systems coincide at $z = z_0$, i.e., $x_0'(x, z_0) = x$ and $y_0(y, z_0) = y$. Propagation to $z = z_1$ would be achieved by multiplying the angular spectrum associated with $v(x_0', y_0', 0)$ (i.e., $V(a_0, b_0, 0)$) according to:

$$V(a_0, b_0, \Delta z_0') = P(a_0, b_0, \Delta z_0')V(a_0, b_0, 0), \tag{32}$$

where $\Delta z_0' = (z_1 - z_0)/M_0(z_1)$. Returning to the global coordinate system at $z = z_1$ entails the change of coordinates:

$$x = M_0(z_1)x_0'(x, z_1) \tag{33}$$
$$y = M_0(z_1)y_0'(y, z_1). \tag{34}$$

An important detail emerges when propagating the field through the second slice beginning at $z = z_1$. In particular, following the same strategy as for propagation through the first slice, I apply the transformation into the primed coordinate system (x_1', y_1', z_1') where $x_1'(x, z_1) = x$ and $y_1'(x, z_1) = y$, meaning that:

$$x_1'(x, z_1) = M_0(z_1)x_0'(x, z_1) \tag{35}$$
$$y_1'(x, z_1) = M_0(z_1)y_0'(y, z_1). \tag{36}$$

After propagation through this slice, the transformation becomes:

$$x_2'(x, z_2) = x = M_1(z_2)M_0(z_1)x_0'(x, z_1) \tag{37}$$
$$y_2'(x, z_2) = y = M_1(z_2)M_0(z_1)y_0'(y, z_1). \tag{38}$$

I can thus write the following general expressions for the coordinate system transformation at the entrance plane $z = z_i$ of a slice:

$$x_i'(x, z_i) = x = x_0'(x, z_1)\prod_{j=0}^{i-1} M_j(z_{j+1}) \tag{39}$$

$$y_i'(y, z_i) = y = y_0'(y, z_1)\prod_{j=0}^{i-1} M_j(z_{j+1}) \tag{40}$$

and

$$M_i(z_{i+1})x_i'(x, z_{i+1}) = x = x_0'(x, z_1)\prod_{j=0}^{i} M_j(z_{j+1}) \tag{41}$$

$$M_i(z_{i+1})y_i'(y, z_{i+1}) = y = y_0'(y, z_1)\prod_{j=0}^{i} M_j(z_{j+1}) \tag{42}$$

for the exit plane $z = z_{i+1}$.

2.1 Outline of algorithm

All of the elements of the MS algorithm introduced in this paper have now been introduced and the algorithm can be explained in its entirety. Assuming a partition of slices as illustrated in Fig. 2, the complex amplitude due to a point source is evaluated analytically on the sampled grid at $z = z_0$, which is immediately transformed into the primed coordinate system according to Eqs. (22)-(25) yielding $\hat{v}(x_0', y_0', z_0'(z_0))$. This field is the base case of a recursive definition of the algorithm which propagates the field in the primed coordinate system to the end of the final slice given as:

$$\begin{aligned}&\hat{v}(\hat{x}_i', \hat{y}_i', z_i'(z_{i+1})) = \\ &\exp\left(\mathrm{i}\phi(M_i(z_{i+1})\hat{x}_i', M_i(z_{i+1})\hat{y}_i')\right)\cdot \\ &\hat{\mathcal{F}}^{-1}\left\{P(\hat{a}_i', \hat{b}_i', z_i'(z_{i+1}))\hat{\mathcal{F}}\left\{\hat{v}(\hat{x}_i', \hat{y}_i', z_i'(z_i))\right\}\right\}.\end{aligned} \tag{43}$$

It is also necessary to make the following assignment when transferring from the end of one slice into the beginning of an adjacent slice:

$$\hat{v}\left(\frac{\hat{x}_{i+1}'}{M_i(z_{i+1})}, \frac{\hat{y}_{i+1}'}{M_i(z_{i+1})}, z_{i+1}'(z_{i+1})\right) = \hat{v}(\hat{x}_i', \hat{y}_i', z_i'(z_{i+1})). \tag{44}$$

At the end of the final slice located at $z = z_{N_s}$, the field in the primed coordinate system, $\hat{v}(\hat{x}_{N_s-1}', \hat{y}_{N_s-1}', z_{N_s-1}'(z_{N_s}))$, must be transformed back to the global coordinate system according to Eqs. (22)-(25). It is worth noting that at each iteration of Eq. (43), $\hat{v}$ is simply a matrix which is continually updated by the DFT and multiplication operations contained within Eq. (43). In particular, no additional operations such as resampling are necessary. Instead, the underlying real space coordinate system vectors are continually being rescaled according to:

$$\hat{x}_i' = \hat{x}_0'\prod_{j=0}^{i-1} M_j(z_{j+1}) \tag{45}$$

$$\hat{y}_i' = \hat{y}_0'\prod_{j=0}^{i-1} M_j(z_{j+1}), \tag{46}$$

where $\hat{x}_0'$ and $\hat{y}_0'$ are established at the beginning of the calculation and it is understood that $\hat{x}_i'$ and $\hat{y}_i'$ correspond to the beginning of the slice $z_i \leq z \leq z_{i+1}$. Furthermore, as is outlined in Sec. 2.2 below, the reciprocal space coordinate system vectors are also constantly being rescaled according to:

$$\hat{a}_i' = \hat{a}_0'/\prod_{j=0}^{i-1} M_j(z_{j+1}) \tag{47}$$

$$\hat{b}_i' = \hat{b}_0'/\prod_{j=0}^{i-1} M_j(z_{j+1}), \tag{48}$$

where $\hat{a}_0'$ and $\hat{b}_0'$ are established at the beginning of the simulation.

2.2 Numerical implementation

The simulation methodology outlined in this paper is designed to be implemented using discrete Fourier transforms. I assume that a divergent spherical wave is incident upon the plane $z = z_0$. After applying the coordinate system transformation into the primed coordinate system, the spatially sampled grid must be defined as indicated in Eq. (12). By

noting that at $z = z_0$ I have $(x'_0, y'_0) = (x, y)$, the sampled grid in the primed coordinate system is defined as:

$$\tilde{x}'_0 = \tilde{y}'_0 = \{(j - N/2)\Delta x | 0 \leq j < N\} \tag{49}$$

and the reciprocal space propagation vectors as:

$$\tilde{a}'_0 = \tilde{b}'_0 = \{\lambda(j - N/2)/(N\Delta x) | 0 \leq j < N\}. \tag{50}$$

The only non-trivial aspect of this algorithm from a numerical point of view is that each time the field is propagated through a slice, the sampled grid (Eq. (49)) is magnified after transformation back to the global coordinate system. For example, after performing angular spectrum propagation and transforming back to the global coordinate system after the first slice, the sampled complex amplitude $\tilde{u}$ will now be implicitly defined on a global coordinate system sampled grid defined by $M_0(z_1)\tilde{x}'_0$ and $M_0(z_1)\tilde{y}'_0$, respectively. In general, using Eqs. (41) and (42), the sampled grid in the global coordinate system at exit plane $z = z_{i+1}$ will be given by $\tilde{x}'_0 \prod_{j=0}^{i} M_j(z_{j+1})$ and $\tilde{y}'_0 \prod_{j=0}^{i} M_j(z_{j+1})$, respectively. This has two principal consequences for the algorithm, the first of these being that at the exit plane $z = z_{i+1}$ the sampled reciprocal space propagation vectors are given by $\tilde{a}'_0 / \prod_{j=0}^{i} M_j(z_{j+1})$ and $\tilde{b}'_0 / \prod_{j=0}^{i} M_j(z_{j+1})$, respectively. The second of these implications is that any band limited projection functions (see Eq. (31)) must be evaluated on a different spatially sampled grid for every slice. In some cases this may not entail significant computational cost. However, in the case of diffracting spheres, for example, where the Fourier transform of the projection function must be evaluated via numerical integration (see Appendix A), direct evaluation of this Fourier transform on a different grid for each slice may be too computationally costly. In this case, however, use can be made of the Fourier transform relationship:

$$t(Mx, My) = \mathcal{F}^{-1}\{T(f_x/M, f_y/M)\}/M^2, \tag{51}$$

meaning that $T_{sphere}\left(\sqrt{f_x^2 + f_y^2}\right)$ must be resampled onto the reciprocal space frequency grid $(\tilde{f}_x/M, \tilde{f}_y/M)$ which may be done efficiently by one-dimensional interpolation of a lookup table. As an additional step, prior to performing inverse Fourier transformation to obtain $t_{sphere}(M\tilde{x}, M\tilde{y})$, it is convenient to multiply $T(f_x/M, f_y/M)$ by $\exp(-i2\pi(\tilde{f}_x x_s + \tilde{f}_y y_s))$ to allow for modelling spheres located at an arbitrary position (x_s, y_s, z_s) where it is assumed that z_s lies within the slice being considered.

2.3 Sampling requirements

I shall define the sampling requirements with reference to a cut-off frequency f_{co} such that the windowing function $W(f_x, f_y)$, assumed to be separable in f_x and f_y, takes the value of 0 for $|f_x| > f_{co}$ and $|f_y| > f_{co}$. From this point on I shall assume that the spatial, and therefore reciprocal, computational grids are entirely isotropic. The first requirement that $\Delta x = \Delta y$ must satisfy is:

$$\Delta x \leq \frac{1}{2f_{co}}. \tag{52}$$

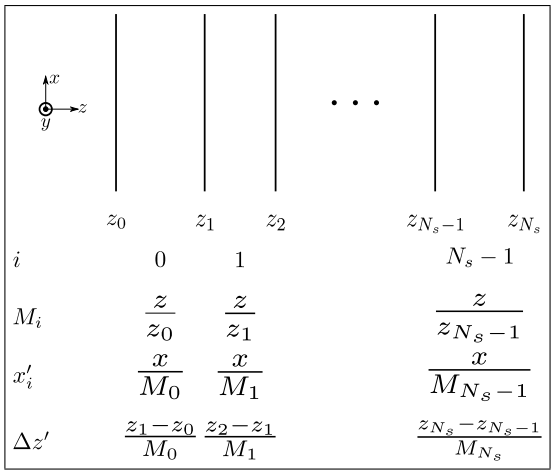

Figure 2: Diagram illustrating the principal coordinate system notation used in this manuscript.

The next requirement is that propagation of the angular spectrum from $z = z_0$ to $z = z_{N_s}$ using Eq. (4) must be correctly sampled in the reciprocal space. Following Matsushima and Shimobaba [11], I find that the sampling period in the reciprocal space, $\Delta f_x = \Delta f_y$ must satisfy:

$$\Delta f_x \leq \frac{z_{N_s}}{2\lambda(z_{N_s} - z_0)z_0 f_{co}}, \tag{53}$$

however, since $\Delta f_x = 1/(N\Delta x)$, this can also be written as:

$$N \geq \frac{2\lambda(z_{N_s} - z_0)z_0 f_{co}}{\Delta x z_{N_s}}. \tag{54}$$

The criteria expressed in Eqs. (52) and (54) do not consider the sampling requirements imposed by diffracting objects. In the case of modelling a single diffracting object, I shall assume that f_{co} is chosen such that the band limited projection function, $t_{BL}(\hat{x}, \hat{y})$, has satisfactory agreement with the actual projection function, $t(x, y)$. I do not propose criteria for making this assessment, however, one can assess this by considering the difference between scattered fields predicted by both treatments. In order to avoid aliasing when using the projection approximation, a guard band of width f_{co} should be employed as illustrated in Fig. 3. Whenever a complex amplitude, $\hat{u}(\hat{x}, \hat{y})$, encounters a diffracting object, $\hat{t}(\hat{x}, \hat{y})$, imposed via the projection approximation, aliasing will not occur if both $\hat{u}$ and $\hat{t}$ do not contain spectral components within the guard band. The field after diffraction, $\hat{u}(\hat{x}, \hat{y})\hat{t}(\hat{x}, \hat{y})$, will in general contain spectral components within the guard band. In order to prevent aliasing at a subsequent diffracting object, the spectral components of the field within the guard band can be filtered out. The energy lost due to such filtering can be monitored to ensure it is kept below a tolerable level, dependent upon the application. In practice however, it has been found in the examples considered in this paper that the amount of energy entering the guard band is negligible meaning that artefacts arising from aliasing are also negligible.

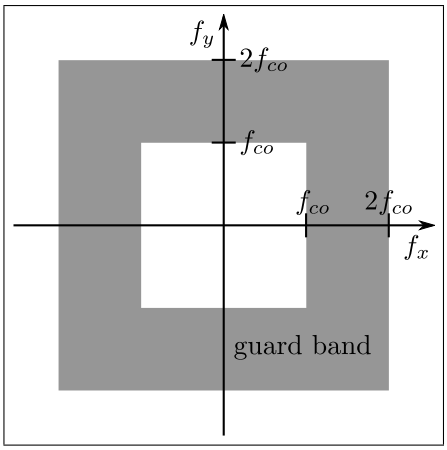

Figure 3: Illustration of the region in reciprocal space (the intersection of $|f_x| < f_{co}$ and $|f_y| < f_{co}$) where the angular spectrum of the field is permitted to reside, along with a guard band where angular spectrum content is filtered after propagation through each layer.

2.4 Non-uniform background refractive indices

Up until this point, for clarity, it has been assumed that all scatterers are contained within free space. It is, however, relatively simple to allow each slice defined by $z_i \leq z \leq z_{i+1}$ to have a background refractive index $n_i = 1 - \delta_i + \mathrm{i}\beta_i$. If the slice contains a refractive index homogeneity as in Eq. (20), this should be redefined as:

$$n(x, y, z) = 1 - (\delta(x, y, z) - \delta_i) + \mathrm{i}(\beta(x, y, z) - \beta_i), \quad (55)$$

recalling that this applies to (x, y, z) inside the inhomogeneity only. The free-space propagation operator (Eq. (4)) must be redefined as:

$$P(a, b, \Delta z) = \exp\left(-\mathrm{i}\frac{k}{1 - \delta_i + \mathrm{i}\beta_i}(a^2 + b^2)\Delta z/2\right). \quad (56)$$

An additional final step must then be applied where the total field exiting the slice must be multiplied by:

$$T_i = \exp(\mathrm{i}k(z_{i+1} - z_i)(-\delta_i + \mathrm{i}\beta_i)), \quad (57)$$

which is necessary because the field $u(x, y, z)$ is considered within the paraxial approximation, meaning that a term $\exp(\mathrm{i}kz)$ is factored out of the field. It is useful to note that the sampled reciprocal space parameters $(\hat{a}'_i, \hat{b}'_i)$ do not require rescaling due to the redefintion of the free-space propagation operator in Eq. (56).

3 Examples and analysis

Code for performing each of the following examples may freely downloaded [12].

3.1 A diffracting aperture

I consider first the simple example of a square diffracting aperture and a monochromatic point source as depicted in Fig. 4 which shows a point source placed 1.6m from a square aperture of width $W = 20\mu$m. The field is observed on the observation plane which is located a further 0.3m from the aperture. The attenuating part of the aperture is assumed to be perfectly attenuating whilst the transmitting region of the aperture is assumed to be perfectly transmitting. The point source is assumed to be monochromatic with photon energy of 20 keV.

The objective of this test is to demonstrate how the choice of N, the number of sample points along each Cartesian direction, impacts upon the accuracy of the simulation method. In particular, for a given choice of N, it remains only to choose either Δx (the isotropic spatial sampling period), or equivalently, X (half the total spatial width of the simulation, see Sec. 1.1). I choose the value of Δx to ensure that, within the primed coordinate system, a spherical wave that has its source in the plane $z = z_a$ is correctly sampled after propagating distance $z' = (z_o - z_a)z_a/z_o$ (see Eq. (25)), resulting in the requirement given by Eq. (14):

$$\Delta x \leq \sqrt{\frac{\lambda(z_o - z_a)z_a}{N z_o}}, \quad (58)$$

where Δx was chosen to have a value of 0.95 of its maximum allowable value. Note that Eq. (58) represents the worst case scenario in which a diffracting object located at $z = z_a$ leads to the creation of a spherical wave within the primed coordinate system. The cut-off frequency, f_{co} is thus dictated by Eq. (52). Increasing the value of N allows for f_{co} to be increased, which reduces the difference between the band limited and true projection functions of the aperture, and later spheres, as explained in Sec. 1.4.

The results of this simulation are shown in Figs. (5) and (6). Figure 5 shows the magnitude of the diffracted field at $z = z_o$ directly evaluated using Fresnel-Kirchhoff diffraction theory as per Eq. (1) of reference [13], without using the primed coordinate system. The field magnitudes as evaluated using primed coordinate system angular spectrum model for $N = 1024, 3072, 5120$ and 7168, appear very similar to that plotted in Fig. 5. As a result, the magnitude of the differences between the complex amplitudes evaluated using the angular spectrum approach and those evaluated directly are plotted in Fig. 6. These plots show that at lower values of N, the diffracted field at $z = z_o$ is spatially truncated as a result of increased filtering of the aperture's projection function. These plots show clearly that increasing N increases the spatial extent over which the calculated diffracted field remains accurate. To further probe the effect that N has upon accuracy, I introduce an error metric defined as:

$$\epsilon = \sqrt{\frac{\sum_{i,j} |u(i\Delta x, j\Delta y) - u_{ref}(i\Delta x, j\Delta y)|^2}{\sum_{i,j} |u_{ref}(i\Delta x, j\Delta y)|^2}}, \quad (59)$$

to quantify the error between complex amplitude $u(i\Delta x, j\Delta y)$ and a reference complex amplitude $u_{ref}(i\Delta x, j\Delta y)$. This error metric is plotted in Fig. 7 where the field calculated using

Fresnel-Kirchhoff diffraction theory is used as the reference field. This plot shows that the error in the field calculated using the primed coordinate system angular spectrum model reduces approximately linearly with the log of N.

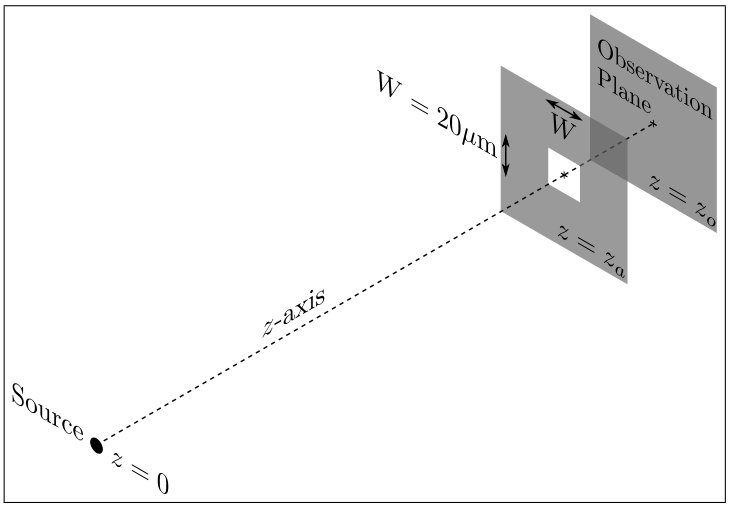

Figure 4: Schematic diagram of the diffracting aperture and point source upon which all examples in Sec. 3 are based. Values of $W = 20\mu$m, $z_a = 1.6$m and $z_o = 1.9$m were chosen. Note that the diagram is not drawn to scale.

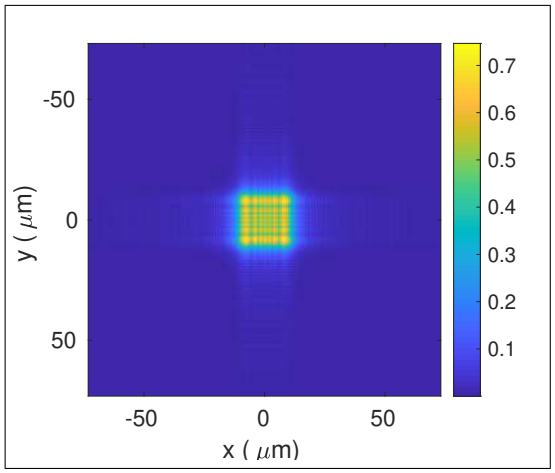

Figure 5: Magnitude of the field diffracted by the aperture found by direct evaluation of the Fresnel-Kirchhoff diffraction integral.

3.2 A diffracting aperture and single sphere

In this example I introduce a single sphere of radius 5μm with $\delta = 2\times10^{-6}$, located a distance 0.1m downstream of the aperture and situated at transverse position $(5, 0)\mu$m relative to the center of the aperture. Following the same method of presentation as in the previous example, the diffracted field found by direct evaluation of the Fresnel-Kirchhoff diffraction integral is plotted in Fig. 5. For the case of a single sphere, a two-dimensional extension of Eq. (8) in reference [13] was used to find the directly evaluated field. The difference between the primed coordinate system angular spectrum model

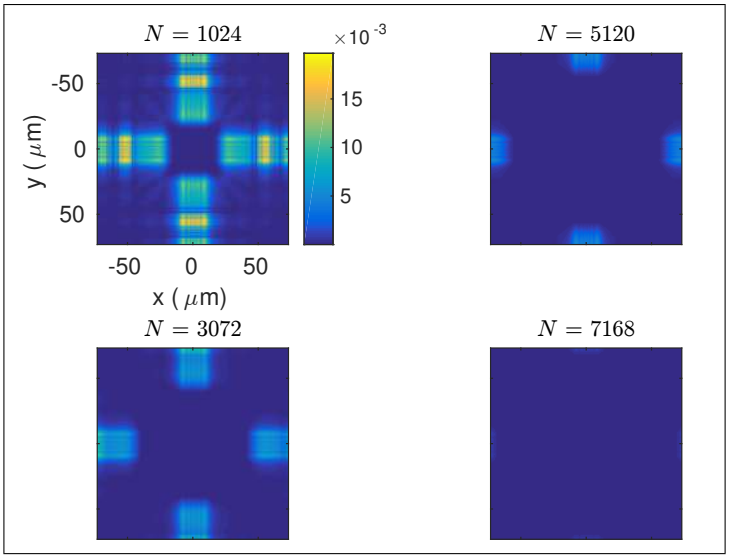

Figure 6: Plots of the magnitude of the error in each calculate complex amplitude relative to that calculated using Fresnel-Kirchhoff diffraction theory for a diffracting aperture.

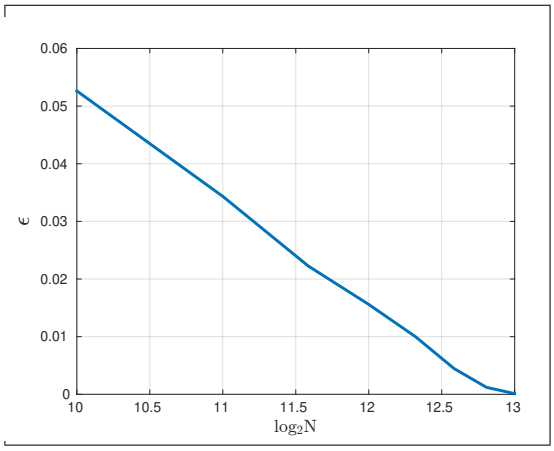

Figure 7: Plot of the error ϵ as a function of N where the reference field is that calculated using Fresnel-Kirchhoff diffraction theory.

and the directly evaluated field is also plotted in Fig. 9, which is seen to be very similar to the case where a sphere was not present. I do not plot the error metric in this case as it was seen to be nearly identical to that which arose in the absence of a sphere, as is plotted in Fig. 7. This example serves the purpose of demonstrating that the primed coordinate system angular spectrum model converges to the directly evaluated field for a reasonably general example.

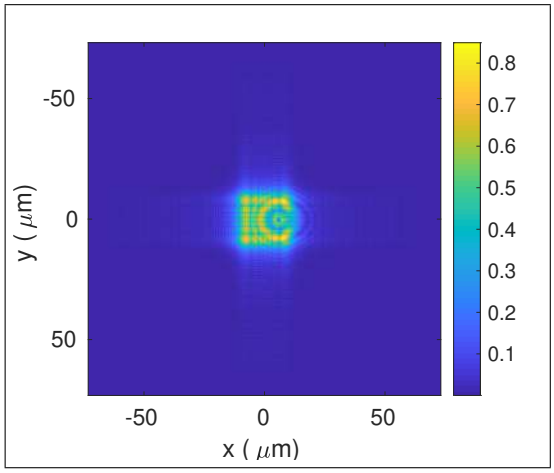

Figure 8: Magnitude of the field diffracted by the aperture and a single sphere found by direct evaluation of the Fresnel-Kirchhoff diffraction integral.

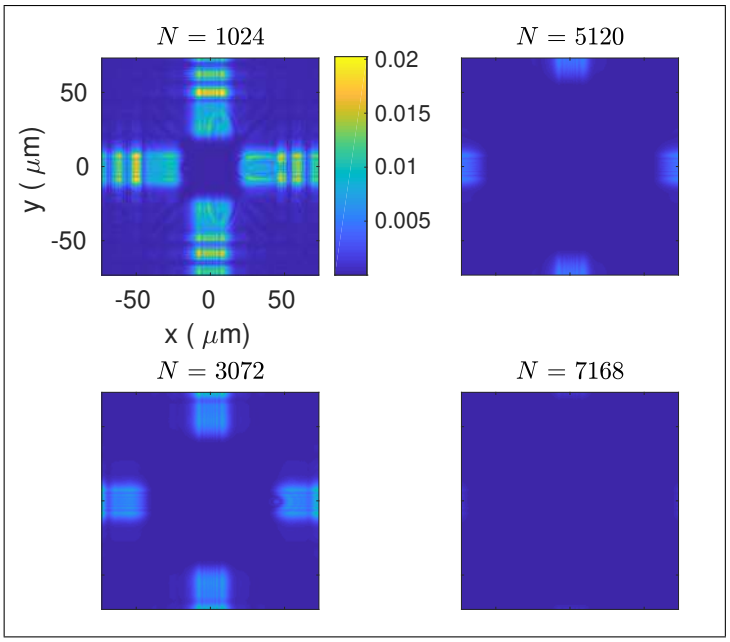

Figure 9: Plots of the magnitude of the error in each calculate complex amplitude relative to that calculated using Fresnel-Kirchhoff diffraction theory for the case of a single sphere and diffracting aperture.

3.3 A diffracting aperture and two spheres

In this example I include an additional sphere with the same radius and δ value as in the previous example, however, located 0.15m down stream of the aperture and at transverse location $(5, 5)\mu$m with respect to the center of the aperture. This example was calculated for the case $N = 7168$ only. The field at the observation plane, calculated using the the primed coordinate system angular spectrum model is shown in the left of Fig. 10. For validation purposes a field was evaluated directly using Fresnel-Kirchhoff diffraction theory. The Fresnel-Kirchhoff field was evaluated by first considering each of the two spheres in isolation. The field resulting from this calculation, as if Born's first-order approximation holds, is shown in the right hand of Fig. 10, which demonstrates that the first-order approximation is not appropriate in this case. The field can be evaluated correctly by taking into account the field which is scattered by both spheres, as is detailed in Appendix B. Once the multiply scattered field is taken into account an error of $\epsilon = 1.2 \times 10^{-3}$ is obtained, thus illustrating the accuracy of the primed coordinate system angular spectrum model.

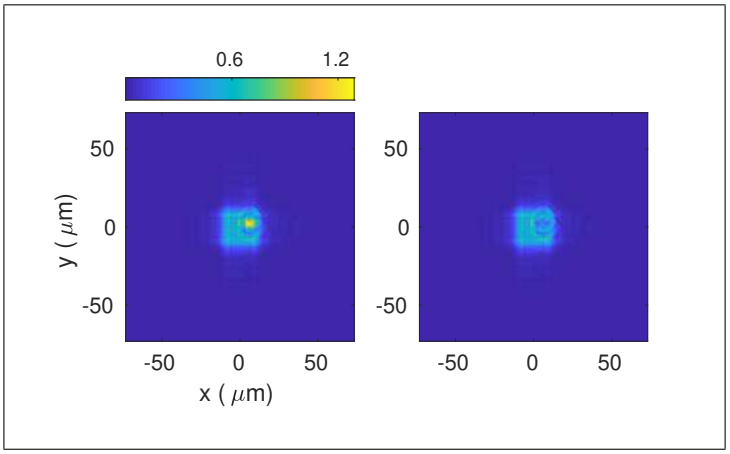

Figure 10: Magnitude of the field obtained when two spheres are located between the aperture and observation plane (left) and the magnitude of the field obtained by considering the two spheres in isolation (right).

3.4 A diffracting aperture and an ensemble of spheres

This final example illustrates the type of application where this model may be particularly useful. Using the same combination of source and aperture as in the previous example, this example considers an ensemble of non-overlapping spheres. Spheres were arranged within a cuboid with a square transverse cross-section of width 100μm and bounded by the planes located 5cm and 10cm, respectively, downstream of the diffracting aperture. A total of 47746 spheres were arranged within this volume resulting in a sphere density of 5% by volume. Although the computation time could have been reduced by considering slices containing multiple spheres, the simulation was performed with one sphere per slice. This was done for two main reasons: to demonstrate how computationally efficient the simulation is, and to ensure the validity of the projection approximation. Simulations were performed for a single ensemble of spheres but each simulation consid-

ered a different value of δ. In any one simulation, each sphere had the same δ value.

The results of the simulation are illustrated in Fig. 11. Each of the four columns in Fig. 11 corresponds to a different value of δ of the spheres, including the free space case. The first row of images shows a somewhat zoomed out view of the field magnitude on the observation plane, whilst the middle row shows a zoomed in view. The lower row of images shows a histogram of the proportion of pixels having field magnitude within a certain range. The bar plots are derived from the pixels within the magnified views of the middle row of images. The line plot shows the distribution of field magnitudes that would be expected from a Rayleigh distribution [14] having mean equal to that of the simulated field distributions shown in the middle row of images. This comparison with the Rayleigh distribution is performed purely to demonstrate that for $\delta = 10^{-6}$, the complex amplitude can be considered to be a fully developed speckle pattern.

3.5 Comparison of computational complexity

The primed coordinate system angular spectrum method is several orders of magnitude more computationally efficient than direct evaluations of the Fresnel-Kirchhoff integral for the case of a single sphere. For multiple spheres direct evaluations of the Fresnel-Kirchhoff integral becomes unfeasible from a computational point of view. This is illustrated in Fig. 12 which plots the computation time per observation point against the number of observation points. This timing information was obtained for the case of a single sphere and a square diffracting aperture as discussed in Sec. 3.2. Simulations were run on a computer containing 512 MB of RAM and two Intel® Xeon® Gold 6148 Processors each possessing 20 physical cores running at 2.40 GHz. I note, however, that only a small proportion of the RAM was used for either simulation. Both simulation techniques were implemented in MATLAB (R2017b) and all 40 physical cores were used. The Fresnel-Kirchhoff method was parallelised trivially by using a `parfor` loop to compute the field at different points in the observation plane in parallel. The primed coordinate system angular spectrum method was parallelised using the parallelisation intrinsic to MATLAB's implementation of the fast Fourier transform (i.e., `fft2`).

Both simulation techniques are seen to exhibit a reduction in the computation per sample point as the number of sample points increases as simulation overheads are amortised over an increasing number of points. The computation time per point for the primed coordinate system angular spectrum method is of the order of $5{\times}10^4$ times lower than that of the Fresnel-Kirchhoff method.

The simulations considered in Sec. 3.4 each required approximately the same computation time, irrespective of the value of δ the spheres were assumed to have. Each computation such as are displayed in Fig. 11 took an average of $6.3{\times}10^4$ seconds to compute. Whilst this may be considered a substantial computation time, such a calculation is intractable using the Fresnel-Kirchhoff formalism. Also, as discussed in Sec. 3.4, this simulation could have been evalu-

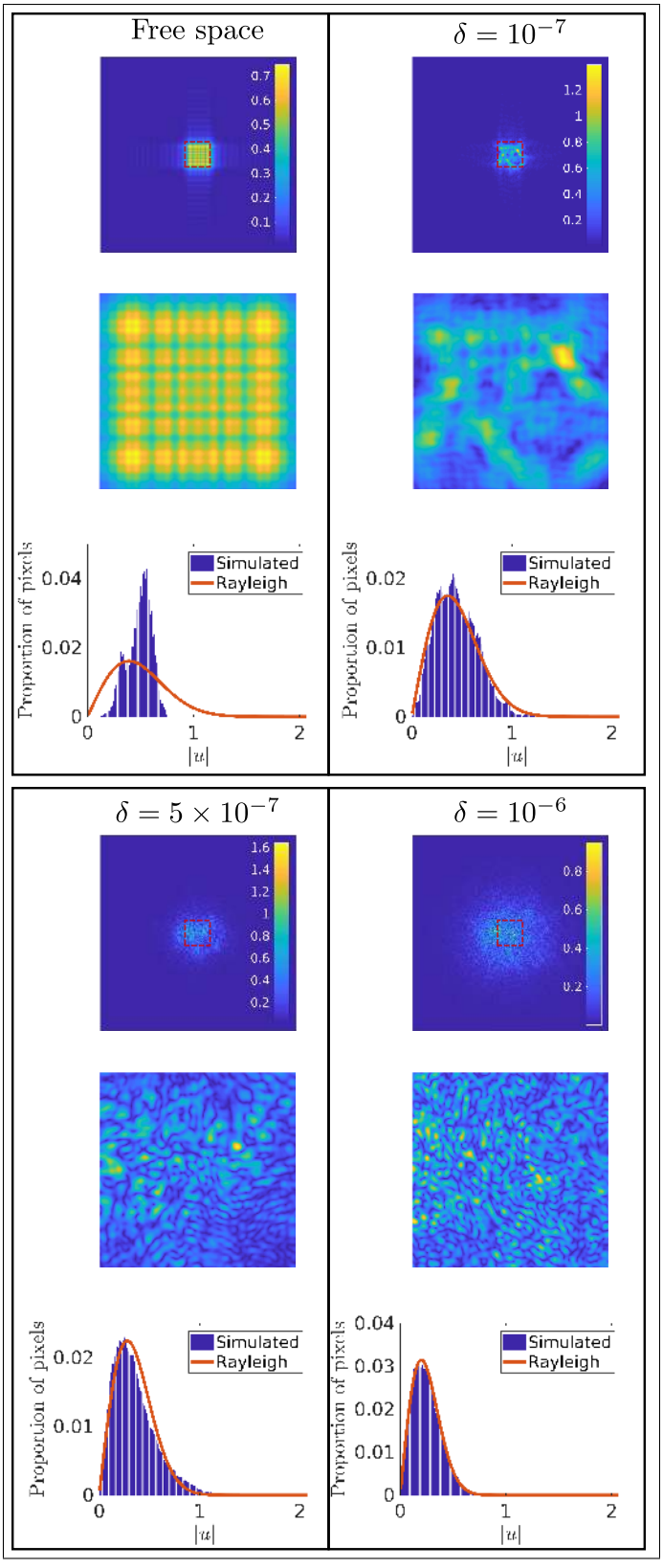

Figure 11: The magnitude of the field that results when an ensemble of spheres is located between a square diffracting aperture and the observation plane. Each group of three images corresponds to a different value of δ for the spheres, including the top left group which represents free space. The middle image in each group is a magnified view of the region denoted by the outline box in the top image. The lowest image shows a histogram of the magnitudes of the pixels within the magnified region along with a Rayleigh distribution with mean equal to that of the magnified region.

ated significantly faster by considering multiple spheres per slice, thus substantially reducing the number of evaluations of `fft2`.

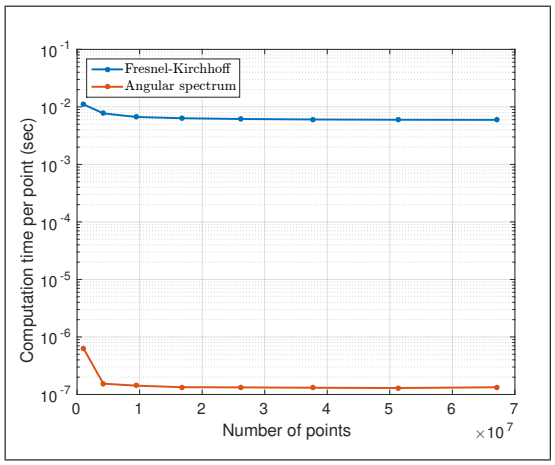

Figure 12: Plots of computation time per sample point in the observation plane for the Fresnel-Kirchhoff and primed coordinate system angular spectrum methods.

4 Conclusions

I have shown how the simulation of divergent beams propagating through axially extended diffracting objects can pose sampling challenges when using Fourier based multi-slice propagation techniques. Two principle solutions to these challenges have been demonstrated. The first of these is to use a divergent-wave to plane-wave transformation which significantly reduces the sampling requirement when simulating the propagation of such beams through homogeneous volumes. The second of these is the calculation of band limited object projection functions which guarantees that aliasing will not occur when using Fourier theory to propagate a beam which has been perturbed by a diffracting object under the projection approximation. Both of these solutions have been combined into a multi-slice simulation technique. I have provided validation of the technique for an example employing a square aperture only and for the case of a square aperture with one or two spheres, respectively. I have also used the technique to simulate beam propagation through an ensemble of spheres dispersed throughout a macroscopic scale volume. I expect this technique to be useful in the study of modalities such as X-ray dark field imaging.

Appendix A: Band limited projection function of a sphere

The projection function of a sphere, located at the origin, with refractive index $n = 1 - \delta + \mathrm{i}\beta$ and radius R is given as:

$$t_{sphere}(x,y) = \begin{cases} \exp(\mathrm{i}k2(-\delta+\mathrm{i}\beta)\sqrt{R^2-x^2-y^2}) & x^2+y^2 \leq R^2 \\ 1 & \text{Otherwise,} \end{cases}$$

and its Fourier transform by:

$$\begin{aligned} T_{sphere}(f_x,f_y) &= \iint_{-\infty}^{\infty} t_{sphere}(x,y)\exp(-\mathrm{i}2\pi(xf_x+yf_y))\mathrm{d}x\mathrm{d}y \\ &= \delta(f_x,f_y)+ \\ &\int_{-\sqrt{R^2-x^2}}^{\sqrt{R^2-x^2}}\int_{-R}^{R}(t_{sphere}(x,y)-1)\exp(-\mathrm{i}2\pi(xf_x+yf_y))\mathrm{d}x\mathrm{d}y, \end{aligned} \tag{60}$$

where $\delta(f_x,f_y)$ is Dirac's delta function. I can simplify Eq. (60) by substituting in polar coordinates for both the spatial and frequency coordinates as:

$$x = \rho\cos\phi \tag{61}$$
$$y = \rho\sin\phi \tag{62}$$
$$f_x = \xi\cos\varphi \tag{63}$$
$$f_y = \xi\sin\varphi, \tag{64}$$

allowing us to write Eq. (60) as:

$$\begin{aligned} T_{sphere}(\xi) &= \delta(f_x,f_y)+ \\ &\int_0^{2\pi}\int_0^{R}(t_{sphere}(\rho)-1)\exp(-\mathrm{i}2\pi\rho\xi\cos(\phi-\varphi))\rho\mathrm{d}\rho\mathrm{d}\phi \\ &= \delta(f_x,f_y) + 2\pi\int_0^{R}(t_{sphere}(\rho)-1)\rho J_0(\rho\xi)\mathrm{d}\rho \end{aligned} \tag{65}$$

where J_0 is the zero-order Bessel function of the first kind. As discussed in Sec. 1.4 the band limited version of $t_{sphere}(x,y)$ is then obtained as:

$$t_{sphere,BL}(\tilde{x},\tilde{y}) = \hat{\mathcal{F}}^{-1}\left\{W(\tilde{f}_x,\tilde{f}_y)T_{sphere}(\sqrt{\tilde{f}_x^2+\tilde{f}_y^2})\right\}, \tag{66}$$

where, recall, that $(\tilde{x},\tilde{y})$ and $(\tilde{f}_x,\tilde{f}_y)$ are the discretised spatial and reciprocal space sample grids, respectively.

Appendix B: Fresnel-Kirchhoff diffraction theory

I consider a complex amplitude incident upon a diffracting object which I define as $u_{inc}(x,y,z)$. I assume that the diffracting object is contained within the planes $z = z_1$ and $z = z_1 + \Delta z_1$. Then I apply the projection approximation, as outline in Sec. 1.1, to obtain the field in the plane $z = z_1+\Delta z_1$ as $u(x,y,z_1+\Delta z_1) = u_{inc}(x,y,z_1+\Delta z_1)\exp(i\phi_1(x,y))$ where $\phi_1(x,y)$ is evaluated according to Eq. (21) with $z_i = z_1$ and $z_{i+1} = z_1+\Delta z$. The field at some arbitrary observation point, down stream of the diffracting object, may then be found according to:

$$\begin{aligned} u(x,y,z_o) = \iint_{-\infty}^{\infty} & K(x,y,x',y',z_o-(z_1+\Delta z_1)) \\ & u_{inc}(x',y',z_1+\Delta z_1)\exp(i\phi_1(x',y'))\mathrm{d}x'\mathrm{d}y', \end{aligned} \tag{67}$$

where K is the Fresnel-Kirchhoff integral kernel given by [13]:

$$K(x,y,x',y',z) = \frac{-\mathrm{i}}{\lambda z}\exp(\mathrm{i}kz)\exp\left(\mathrm{i}k\frac{(x-x')^2+(y-y')^2}{2z}\right). \tag{68}$$

The integral in Eq. (67) must be evaluated over an infinite plane which is unsuitable for numerical integration. Instead, an often used technique is to rewrite the integral as:

$$u(x,y,z_o) = u_{inc}(x,y,z_o) + \iint_{\Omega_1} K(x,y,x',y',z_o-(z_1+\Delta z_1)) \cdot u_{inc}(x',y',z_1+\Delta z_1)\big(\exp(i\phi_1(x',y'))-1\big)\mathrm{d}x'\mathrm{d}y', \tag{69}$$

where $u_{inc}(x',y',z_o)$ is the field incident directly on (x,y,z_o) in the absence of the diffracting aperture and Ω_1 is the transverse extent of the diffracting object. Using this approach the concept of the scattered field, $u_{sc}(x,y,z_o)$, can be defined by decomposing $u(x,y,z_o)$ as:

$$u(x,y,z_o) = u_{inc}(x,y,z_o) + u_{sc}(x,y,z_o). \tag{70}$$

If now a second diffracting object is introduced within the planes $z=z_2$ and $z=z_2+\Delta z_2$, with $z_1+\Delta z_1 \le z_2 \le z_2+\Delta z_2 \le z_o$, the field at (x,y,z_o) may be found by evaluating Eq. (69), by noting that the field incident upon the second sphere is given as $u(x,y,z_2) = u_{inc}(x,y,z_2)+u_{sc}(x,y,z_2)$, which allows the field on the observation plane to be evaluated as:

$$u(x,y,z_o) = u_{inc}(x,y,z_o) + u_{sc}(x,y,z_o) + \iint_{\Omega_2} K(x,y,x',y',z_o-(z_2+\Delta z_2)) \big(u_{inc}(x',y',z_2+\Delta z_2)+u_{sc}(x',y',z_2+\Delta z_2)\big) \big(\exp(i\phi_2(x',y'))-1\big)\mathrm{d}x'\mathrm{d}y'. \tag{71}$$

Up until this point, I have used the notation $u_{sc}(x,y,z)$ to refer to the field scattered by the first diffracting object only. In order to avoid confusion, I now introduce $u_{sc,1}(x,y,z_o)$ and $u_{sc,2}(x,y,z_o)$ which refer to the fields scattered by the two diffracting objects, respectively, each in isolation. This allows the field due to two diffracting objects to be decomposed as:

$$u(x,y,z_o) = u_{inc}(x,y,z_o) + u_{sc,1}(x,y,z_o) + u_{sc,2}(x,y,z_o) + u_{sc,sc}(x,y,z_o), \tag{72}$$

where $u_{inc}(x,y,z_o)$ is the field directly incident in the absence of any diffracting objects and $u_{sc,sc}(x,y,z_o)$ is the multiply scattered field.

Acknowledgements

P. M. is supported by a Royal Society University Research Fellowship. This work was partially supported by EPSRC grant EP/P005209/1.

References

[1] J. M. Cowley and A. F. Moodie, "The scattering of electrons by atoms and crystals. i. a new theoretical approach," Acta Crystallographica **10**, 609–619 (1957).

[2] A. Hare and G. Morrison, "Near-field soft x-ray diffraction modelled by the multislice method," Journal of Modern Optics **41**, 31–48 (1994).

[3] Y. Wang, "A numerical study of resolution and contrast in soft x-ray contact microscopy," Journal of Microscopy **191**, 159–169 (1998).

[4] A. Malecki, G. Potdevin, and F. Pfeiffer, "Quantitative wave-optical numerical analysis of the dark-field signal in grating-based x-ray interferometry," Europhysics Letters **99**, 48001 (2012).

[5] K. Li, M. Wojcik, and C. Jacobsen, "Multislice does it all-calculating the performance of nanofocusing x-ray optics," Opt. Express **25**, 1831–1846 (2017).

[6] D. Paganin, Coherent X-ray optics, (Oxford University Press, 2006).

[7] J. Goodman, Introduction to Fourier Optics (McGraw-Hill, 2005).

[8] E. A. Sziklas and A. E. Siegman, "Mode calculations in unstable resonators with flowing saturable gain. 2: Fast Fourier transform method," Appl. Opt. **14**, 1874–1889 (1975).

[9] E. A. Sziklas and A. E. Siegman, "Diffraction calculations using fast Fourier transform methods," Proceedings of the IEEE **62**, 410–412 (1974).

[10] K. S. Morgan, K. K. W. Siu, and D. M. Paganin, "The projection approximation and edge contrast for x-ray propagation-based phase contrast imaging of a cylindrical edge," Opt. Express **18**, 9865–9878 (2010).

[11] K. Matsushima and T. Shimobaba, "Band-limited angular spectrum method for numerical simulation of free-space propagation in far and near fields," Opt. Express **17**, 19662–19673 (2009).

[12] P. R. T. Munro, "Multi-slice x-ray beam propagation code," http://prtmunro.net.

[13] P. R. T. Munro, K. Ignatyev, R. Speller, and A. Olivo, "The relationship between wave and geometrical optics models of coded aperture type x-ray phase contrast imaging systems," Opt. Express **18**, 4103–4117 (2010).

[14] J. W. Goodman, Laser Speckle and Related Phenomena (Springer-Verlag, 1975).